Carbon star formation as seen through the non-monotonic initial–final mass relation

ARTICLES
https://doi.org/10.1038/s41550-020-1132-1

nature astronomy

Check for updates

Carbon star formation as seen through the non-monotonic initial–final mass relation

Paola Marigo[1]✉, Jeffrey D. Cummings[2], Jason Lee Curtis[3,4], Jason Kalirai[5,6], Yang Chen[1], Pier-Emmanuel Tremblay[7], Enrico Ramirez-Ruiz[8], Pierre Bergeron[9], Sara Bladh[1,10], Alessandro Bressan[11], Léo Girardi[12], Giada Pastorelli[1,6], Michele Trabucchi[1,13], Sihao Cheng[2], Bernhard Aringer[1] and Piero Dal Tio[1,12]

The initial–final mass relation (IFMR) links the birth mass of a star to the mass of the compact remnant left at its death. While the relevance of the IFMR across astrophysics is universally acknowledged, not all of its fine details have yet been resolved. A new analysis of a few carbon–oxygen white dwarfs in old open clusters of the Milky Way led us to identify a kink in the IFMR, located over a range of initial masses, $1.65 \lesssim M_i/M_\odot \lesssim 2.10$. The kink's peak in white dwarf mass of about 0.70–0.75 $M_\odot$ is produced by stars with $M_i \approx 1.8$–$1.9\,M_\odot$, corresponding to ages of about 1.8–1.7 Gyr. Interestingly, this peak coincides with the initial mass limit between low-mass stars that develop a degenerate helium core after central hydrogen exhaustion, and intermediate-mass stars that avoid electron degeneracy. We interpret the IFMR kink as the signature of carbon star formation in the Milky Way. This finding is critical to constraining the evolution and chemical enrichment of low-mass stars, and their impact on the spectrophotometric properties of galaxies.

Carbon is essential to life on Earth, but its origin in the Milky Way is still debated: some studies[1,2] place the major site of its synthesis in the winds of massive stars that eventually exploded as supernovae, others[3,4] are in favour of low-mass stars that blew off their envelopes by stellar winds and became white dwarfs (WDs). Within the latter group, the primary sources of carbon are the winds of carbon stars, characterized by a photospheric carbon-to-oxygen ratio C/O > 1, which form during the thermally pulsing asymptotic giant branch (TP-AGB) phase as a consequence of repeated third dredge-up (3DU) episodes. So far, the range of initial masses of carbon stars and their chemical ejecta are not accurately known from theory[5] as these quantities depend on a number of complex physical processes that are difficult to model, convection and mass loss above all.

Here we show that the initial–final mass relation (IFMR) of WDs may help shed light on this matter. The IFMR connects the mass of a star on the main sequence, M_i, with the mass, M_f, of the WD left at the end of its evolution. This fate[6] is common to low- and intermediate-mass stars ($0.9 \lesssim M_i/M_\odot \lesssim 6$–$7$) that, after the exhaustion of helium in the core, go through the AGB phase and produce carbon–oxygen WDs. The IFMR is also useful to investigate the quasi-massive stars ($8 \lesssim M_i/M_\odot \lesssim 10$) that, after the carbon burning phase, evolve as super-AGB stars and eventually produce oxygen–neon–magnesium WDs.

The IFMR plays a key role in several fields of modern astrophysics[7]. Once M_i is known, the IFMR fixes the mass of the metal-enriched gas returned to the interstellar medium, thus putting constraints to the efficiency of stellar winds during the previous evolution. The high-mass end of the IFMR provides an empirical test to determine the maximum initial mass for stars that develop degenerate neon–oxygen–magnesium cores and proceed through the super-AGB phase without exploding as electron-capture supernovae. The IFMR is also relevant in a wider framework as a key ingredient in chemical evolution models of galaxies; at the same time, it sets a lower limit to the nuclear fuel burnt during the TP-AGB, therefore constraining the contribution of this phase to the integrated light of galaxies[8–10].

To derive the semi-empirical IFMR, singly evolved WDs that are members of star clusters are ideally used[11–13]. Spectroscopic analysis provides their atmospheric parameters, that is, surface gravity, effective temperature and chemical composition. Coupling this information to appropriate WD cooling models provides the WD mass, its cooling age, and additional parameters for testing cluster membership and single-star status. Finally, subtracting a WD's cooling age from its cluster's age gives the evolutionary lifetime of its progenitor, and hence its M_i.

Previous analyses[12,14] of old open clusters with ages $\gtrsim$1.5 Gyr (NGC 6121, NGC 6819 and NGC 7789) explored WDs that recently evolved from stars with $M_i < 2\,M_\odot$, and this showed possible signatures of nonlinearity in the IFMR near $M_i \approx 2\,M_\odot$. Updated analyses of these 12 WDs using improved models and uniformly analysed cluster parameters[15], and the addition of 7 WDs in the old open cluster M67[16,17], further supported that the low-mass IFMR is nonlinear and potentially not even monotonically increasing.

The IFMR kink. Compared with the previous studies just mentioned, this study introduces two novel elements: (1) the discovery

[1]Department of Physics and Astronomy G. Galilei, University of Padova, Padova, Italy. [2]Center for Astrophysical Sciences, Johns Hopkins University, Baltimore, MD, USA. [3]Department of Astrophysics, American Museum of Natural History, New York, NY, USA. [4]Department of Astronomy, Columbia University, New York, NY, USA. [5]Johns Hopkins University Applied Physics Laboratory, Laurel, MD, USA. [6]Space Telescope Science Institute, Baltimore, MD, USA. [7]Department of Physics, University of Warwick, Coventry, UK. [8]Department of Astronomy and Astrophysics, University of California, Santa Cruz, CA, USA. [9]Département de Physique, Université de Montréal, Montréal, Quebec, Canada. [10]Theoretical Astrophysics, Department of Physics and Astronomy, Uppsala University, Uppsala, Sweden. [11]International School for Advanced Studies, Trieste, Italy. [12]Astronomical Observatory of Padova – INAF, Padova, Italy. [13]Department of Astronomy, University of Geneva, Versoix, Switzerland. ✉e-mail: paola.marigo@unipd.it

Table 1 | Main parameters of the WDs and their stellar progenitors

Name	RA (h:min:s)	Dec (°:′:″)	$T_{\mathrm{eff_S}}$ (K)	$\log g_S$ (cm s^{-2})	$M_{\mathrm{f_S}}$ ($M_\odot$)	M_G (mag)	$M_{\mathrm{f_P}}$ ($M_\odot$)	M_f ($M_\odot$)	τ (Myr)	M_i ($M_\odot$)
DA members										
R147-WD01	19:15:33.8	−16:52:49	17,850 ± 250	8.11 ± 0.04	0.69 ± 0.03	11.08 ± 0.05	0.66 ± 0.02	0.67 ± 0.02	129^{+11}_{-9}	$1.66^{+0.01}_{-0.01}$
R147-WD04	19:16:59.7	−16:31:21	19,550 ± 250	8.07 ± 0.04	0.66 ± 0.03	10.93 ± 0.05	0.67 ± 0.02	0.67 ± 0.02	92^{+10}_{-8}	$1.65^{+0.01}_{-0.01}$
R147-WD07	19:16:13.7	−16:20:13	15,900 ± 200	8.08 ± 0.04	0.66 ± 0.03	11.35 ± 0.05	0.68 ± 0.02	0.67 ± 0.02	193^{+13}_{-11}	$1.68^{+0.01}_{-0.01}$
R147-WD08	19:18:44.3	−15:53:56	13,000 ± 200	8.11 ± 0.05	0.67 ± 0.03	11.78 ± 0.05	0.70 ± 0.03	0.69 ± 0.02	368^{22}_{-21}	$1.73^{+0.01}_{-0.01}$
R147-WD10	19:18:01.7	−15:49:56	17,950 ± 250	8.08 ± 0.04	0.67 ± 0.03	11.14 ± 0.05	0.69 ± 0.02	0.68 ± 0.02	131^{+11}_{-9}	$1.66^{+0.01}_{-0.01}$
N752-WD01	01:59:05.5	+38:03:38	15,500 ± 250	8.12 ± 0.04	0.69 ± 0.03	11.26 ± 0.05	0.62 ± 0.02	0.65 ± 0.02	191^{+15}_{-14}	$2.10^{+0.02}_{-0.02}$
DB member										
R147-WD02	19:12:52.5	−16:14:35	16,300 ± 200	8.12 ± 0.05	0.67 ± 0.03	11.23 ± 0.05	0.66 ± 0.02	0.66 ± 0.02	188^{+13}_{-10}	$1.68^{+0.01}_{-0.01}$
Non-members										
R147-WD03	19:18:58.2	−16:48:22	15,300 ± 250	8.00 ± 0.04	0.61 ± 0.03	-	-	-	185^{+16}_{-15}	-
R147-WD09	19:15:03.7	−16:03:41	15,800 ± 200	7.96 ± 0.04	0.59 ± 0.02	-	-	-	155^{+14}_{-13}	-
R147-WD11	19:14:38.1	−15:58:58	14,900 ± 200	8.00 ± 0.04	0.61 ± 0.03	-	-	-	202^{+17}_{-16}	-
R147-WD15	19:15:18.2	−17:37:10	-	-	-	-	-	-	-	-
Name	**RA (h:min:s)**	**Dec (°:′:″)**	**$T_{\mathrm{eff_S}}$ (K)**	**$\log g_S$ (cm s^{-2})**	**$M_{\mathrm{f_S}}$ ($M_\odot$)**	**M_V (mag)**	**$M_{\mathrm{f_P}}$ ($M_\odot$)**	**M_f ($M_\odot$)**	**τ (Myr)**	**M_i ($M_\odot$)**
Previous low-mass WD parameters updated with photometric analysis										
M4-WD00	16:23:49.9	−26:33:32	20,900 ± 500	7.77 ± 0.08	0.51 ± 0.04	10.57 ± 0.15	0.59 ± 0.06	0.53 ± 0.03	37^{+6}_{-4}	$0.87^{+0.01}_{-0.01}$
M4-WD04	16:23:51.3	−26:33:04	25,450 ± 550	7.78 ± 0.07	0.52 ± 0.03	9.94 ± 0.15	0.51 ± 0.05	0.52 ± 0.03	16^{+1}_{-1}	$0.87^{+0.01}_{-0.01}$
M4-WD05	16:23:41.4	−26:32:53	28,850 ± 500	7.77 ± 0.07	0.53 ± 0.03	9.96 ± 0.15	0.61 ± 0.06	0.55 ± 0.03	10^{+1}_{-1}	$0.87^{+0.01}_{-0.01}$
M4-WD06	16:23:42.3	−26:32:39	26,350 ± 500	7.90 ± 0.07	0.59 ± 0.04	9.90 ± 0.15	0.52 ± 0.05	0.56 ± 0.03	14^{+2}_{-1}	$0.87^{+0.01}_{-0.01}$
M4-WD15	16:23:51.0	−26:31:08	24,600 ± 600	7.89 ± 0.08	0.57 ± 0.04	9.98 ± 0.15	0.50 ± 0.05	0.54 ± 0.03	18^{+3}_{-2}	$0.87^{+0.01}_{-0.01}$
M4-WD20	16:23:46.5	−26:30:32	21,050 ± 550	7.79 ± 0.08	0.52 ± 0.04	10.26 ± 0.15	0.49 ± 0.05	0.50 ± 0.03	33^{+5}_{-3}	$0.87^{+0.01}_{-0.01}$
M4-WD24	16:23:41.2	−26:29:54	26,250 ± 500	7.79 ± 0.07	0.53 ± 0.03	9.97 ± 0.15	0.55 ± 0.05	0.54 ± 0.03	14^{+1}_{-1}	$0.87^{+0.01}_{-0.01}$
N6819-6	19:41:20.0	+40:02:56	21,700 ± 350	7.94 ± 0.05	0.60 ± 0.03	10.49 ± 0.10	0.58 ± 0.04	0.59 ± 0.02	40^{+8}_{-5}	$1.61^{+0.01}_{-0.01}$
N7789-5	23:56:49.1	+56:40:13	31,700 ± 450	8.12 ± 0.06	0.71 ± 0.04	9.96 ± 0.10	0.69 ± 0.04	0.70 ± 0.03	8^{+1}_{-1}	$1.90^{+0.01}_{-0.01}$
N7789-8	23:56:57.2	+56:40:01	24,800 ± 550	8.11 ± 0.07	0.70 ± 0.04	10.62 ± 0.10	0.73 ± 0.04	0.71 ± 0.03	35^{+8}_{-5}	$1.91^{+0.01}_{-0.01}$
N7789-11	23:56:30.8	+56:37:19	20,500 ± 650	8.27 ± 0.10	0.79 ± 0.06	10.83 ± 0.10	0.67 ± 0.04	0.70 ± 0.03	81^{+16}_{-15}	$1.94^{+0.02}_{-0.02}$
N7789-14	23:56:37.8	+56:39:08	21,100 ± 950	7.99 ± 0.14	0.62 ± 0.08	11.02 ± 0.10	0.77 ± 0.04	0.74 ± 0.04	85^{+21}_{-18}	$1.94^{+0.02}_{-0.02}$

The parameters for the spectroscopically observed Ruprecht 147 and NGC 752 WD candidates are organized by atmospheric composition (DA/DB) and membership, including the apparent background star R147-WD15. Updated parameters of previously published low-mass WDs are also given. Columns from left to right are WD name, right ascension, declination, spectroscopic-based effective temperature, logarithm of spectroscopic-based surface gravity, spectroscopic-based final mass, photometric-based absolute magnitude, photometric-based final mass, weighted-average final mass, weighted-average WD cooling age and the progenitor's initial mass. The spectroscopic-based errors are from fitting and external errors. The photometric-based errors are from photometric and cluster-parameter errors. For stars classified as non-members of Ruprecht 147, cluster-related parameters are unknown and hence appear as empty cells in the table. The background star R147-WD15 was recognized not to be a WD and therefore no spectroscopic parameter was derived.

of seven WD members of the old open clusters NGC 752 (age ~1.55 Gyr) and Ruprecht 147 (age ~2.5 Gyr); and (2) the use of a new analysis technique that combines photometric and spectroscopic data to better constrain the WD parameters. The same technique is applied both to the 7 newly discovered WDs and to reanalyse 12 previously published WDs with $M_i < 2.1\,M_\odot$ (Table 1). Our new methodology is detailed and discussed in Methods.

These data establish a low-mass IFMR kink across the interval $1.65 \lesssim M_i/M_\odot \lesssim 2.10$, as shown in Fig. 1. All clusters involved in the IFMR kink have near-solar metallicity, $-0.1 \lesssim [\mathrm{Fe/H}] \lesssim 0.1$.

While the steep increase in the IFMR near $M_i \approx 1.65\,M_\odot$ is at present well constrained, further data are needed to better probe the decreasing IFMR for $M_i \gtrsim 2\,M_\odot$. However, we underline that after this rapid increase, such a temporary decrease is necessary to keep consistency with the observed field WD mass distribution. For example, if this steep increase was instead followed by a plateau at $M_f \approx 0.7\,M_\odot$, then every progenitor with $1.9 \lesssim M_i/M_\odot \lesssim 2.8$ would create an ~$0.7\,M_\odot$ WD, substantially overproducing field WDs at this mass compared with observations[15,18]. This aspect is thoroughly discussed in the Supplementary Information (see 'The WD mass distribution'; see also Supplementary Figs. 1 and 2). The kink also illustrates a limitation of inferring the IFMR directly from such field WD mass distributions because a monotonic form must be assumed, for example, using the Gaia Data Release 2 (DR2)[19].

Physical interpretation. We interpret the kink in the IFMR as the signature of the lowest-mass stars in the Milky Way that became carbon stars during the TP-AGB phase. The inflection point near $1.65\,M_\odot$ (Fig. 1) should mark the minimum initial mass for a solar-metallicity star to become a carbon star as a consequence of the 3DU episodes during thermal pulses (TP).

The proposed explanation is as follows. At solar-like metallicity, low-mass carbon stars ($1.65 \lesssim M_i/M_\odot \lesssim 1.90$) attain low C/O ratios ($\lesssim$1.3) and low values of the excess of carbon compared with oxygen, C − O, in the atmosphere. The quantity C − O is particularly relevant as it measures the budget of free carbon, not locked in the CO molecule, available to condense into dust grains. In fact, state-of-the-art dynamical models for carbon stars[20–22] predict

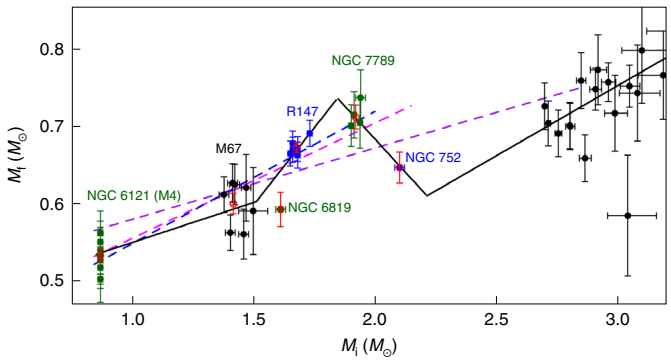

Fig. 1 | The semi-empirical IFMR. The data include the 7 newly discovered WDs (blue data) and the 12 previously published WDs (green data) reanalysed with a method that couples spectroscopy, photometry and the Gaia-based distances of the host star clusters (see Methods for more details). In addition, previous intermediate-mass data and the M67 data are shown in black. Error bars cover a range of $\pm1\sigma$ (see Table 1). Each WD group's cluster is also labelled and each of their parameter averages is overlaid in open red data points. On the basis of these IFMR data and their 1σ error, we illustrate three weighted linear fits, namely: from M_i of 0.85 $M_\odot$ to 2.85 $M_\odot$ (purple dashed line), from M_i of 0.85 $M_\odot$ to 2.15 $M_\odot$ (magenta dashed line), and from M_i of 0.85 $M_\odot$ to 2.00 $M_\odot$ (blue dashed line). As discussed in the Methods, these three fits provide poor representations of the observed data. Conversely, the four-piece linear fit (black), which draws a kink in M_f around $M_i \approx 1.8\,M_\odot$, does provide a strong representation of the data and is our observational IFMR.

that a minimum carbon excess, $(C-O)_{min}$, is necessary to generate dust-driven winds, with mass-loss rates exceeding a few $10^{-7}\,M_\odot\,yr^{-1}$. We recall that according to a standard notation, $C-O = \log(n_C - n_O) - \log(n_H) + 12$, where n_C, n_O and n_H denote the number densities of carbon, oxygen and hydrogen, respectively. More details about the wind models for carbon stars, $(C-O)_{min}$, and our CDYN prescription for mass loss are provided in Methods.

The existence of a threshold in carbon excess impacts on the TP-AGB evolution and hence on the IFMR. In TP-AGB stars, the surface enrichment of carbon is controlled by the 3DU, a series of mixing episodes that happen each time the base of the convective envelope is able to penetrate into the intershell region left at the quenching of a thermal pulse[6]. The efficiency of a 3DU event is commonly described by the dimensionless parameter $\lambda = \Delta M_{3DU}/\Delta M_c$, defined as the amount of dredged-up material, ΔM_{3DU}, relative to the growth of the core mass, ΔM_c, during the previous interpulse period.

Figure 2 illustrates how the efficiency of 3DU regulates the increase of the surface C/O and hence the carbon excess; how the latter, in turn, affects the mass-loss rate, hence the lifetime of a carbon star and eventually the final mass of the WD. The models refer to a star with $M_i = 1.8\,M_\odot$ and metallicity $Z = 0.014$, near the kink's peak of the semi-empirical IFMR. The two cases in Fig. 2a,b share the same set of input prescriptions, except that the 3DU is shallow in the model of Fig. 2a ($\lambda \approx 0.17$), and much more efficient in the model of Fig. 2b ($\lambda = 0.5$ as the star becomes carbon rich). In both cases, as soon as the star reaches C/O > 1, a sudden drop in the mass-loss rate is expected to occur.

This prediction deserves to be explained in detail. The transition from C/O < 1 to C/O > 1 marks a radical change both in the molecular abundance pattern of the atmosphere (shifting from oxygen-bearing to carbon-bearing species)[23], and in the mineralogy of the dust that could in principle condense in the coolest layers.

When a carbon star is born, the silicate-type dust that characterizes the circumstellar envelopes of M-type stars is no longer produced and the composition of the grains that may actually form suddenly changes, switching mainly to silicon carbide and amorphous carbon[24–27]. The key point is that the growth of carbonaceous dust requires suitable physical conditions[25,28] (for example, temperature, density and chemical composition of the gas, stellar radiation field), and these may not always be fulfilled as soon as C/O $\gtrsim$ 1. In addition, carbonaceous grains are expected to drive a wind only if they form in a sufficient amount[20–22], a condition expressed by the threshold $(C-O)_{min}$.

It follows that, as long as the atmospheric abundance of free carbon is small, typically during the early carbon-star stages, dust grains cannot be abundantly produced. This circumstance is clearly shown by computations[24] of dust-grain growth as a function of C/O and mass-loss rate. As we see in Fig. 3, the condensation factor of carbon, f_c, is extremely low for C/O in a narrow range just above unity, irrespective of the mass-loss rate. The inefficiency of the carbon dust condensation extends to larger C/O for low mass-loss rates ($\dot{M} \lesssim 3\times10^{-7}\,M_\odot\,yr^{-1}$). It should be kept in mind that the map of f_c corresponds to a pre-built grid of ($\dot{M}$, C/O) combinations, and clearly not all of them represent realistic cases.

At the same time, such a map is very useful when analysing observed combinations of ($\dot{M}$, C/O), such as those referring to a sample[29] of carbon-rich irregular and semi-regular variables (SRVs). According to our interpretation, these variables should represent the progenitors of the WDs that populate the IFMR kink. For an extensive discussion about this point, see the Supplementary Section 'Other supporting evidence: Galactic semi-regular variables' (see also Supplementary Figs. 4–6).

In Fig. 3, most of the observed SRVs fall in a region of low mass-loss rate and small carbon enrichment, for which we expect an inefficient dust condensation of carbon grains. The natural conclusion is that if carbonaceous dust grains are not abundant enough to drive a powerful wind, when C/O just exceeds unity, then only a modest outflow may be generated, possibly sustained by small-amplitude pulsations, like those of SRV stars[30,31].

These conditions apply to the model of Fig. 2a, which experiences a shallow 3DU. The C/O ratio grows slowly (maximum of ~1.33), the star stays in a phase of very low mass loss until the threshold in carbon excess is slightly overcome and a moderate dust-driven wind is eventually activated, with mass-loss rates not exceeding few $10^{-6}\,M_\odot\,yr^{-1}$. Also the model shown in Fig. 2b enters a phase of low mass loss soon after the transition to carbon star, but then its evolution proceeds differently. As the 3DU is more efficient, C/O increases more rapidly (maximum of ~1.91) so that the threshold in carbon excess is largely overcome, a powerful dust-driven wind is generated and the mass-loss rate increases up to $\sim10^{-5}\,M_\odot\,yr^{-1}$.

These model differences affect the carbon star lifetimes and, in turn, the final masses left after the TP-AGB phase. In the model of Fig. 2a, the carbon star phase lasts ~1.15 Myr and produces a WD with a final mass of ~0.732 $M_\odot$. In model of Fig. 2b, the duration of the carbon star phase is halved, ~0.52 Myr, and terminates with a WD mass of ~0.635 $M_\odot$.

Likewise, shorter lifetimes and lower final masses are obtained if we adopt mass-loss formulations that do not depend on the carbon abundance. In Fig. 2c,d, we show two examples in which we use the B95 and VW93 relations. Both predict a systematic increase of the average mass-loss rate as the star evolves on the TP-AGB. The resulting WD masses are 0.646 $M_\odot$ and 0.615 $M_\odot$, respectively.

The IFMR and carbon star formation in the Milky Way. While the above considerations, relative to a given TP-AGB model, provide the physical key to interpret the data, we aim to build up an overall picture as a function of the initial mass of the star.

Therefore, we employ the large model grid introduced in Methods, which consists of TP-AGB calculations that cover a relevant

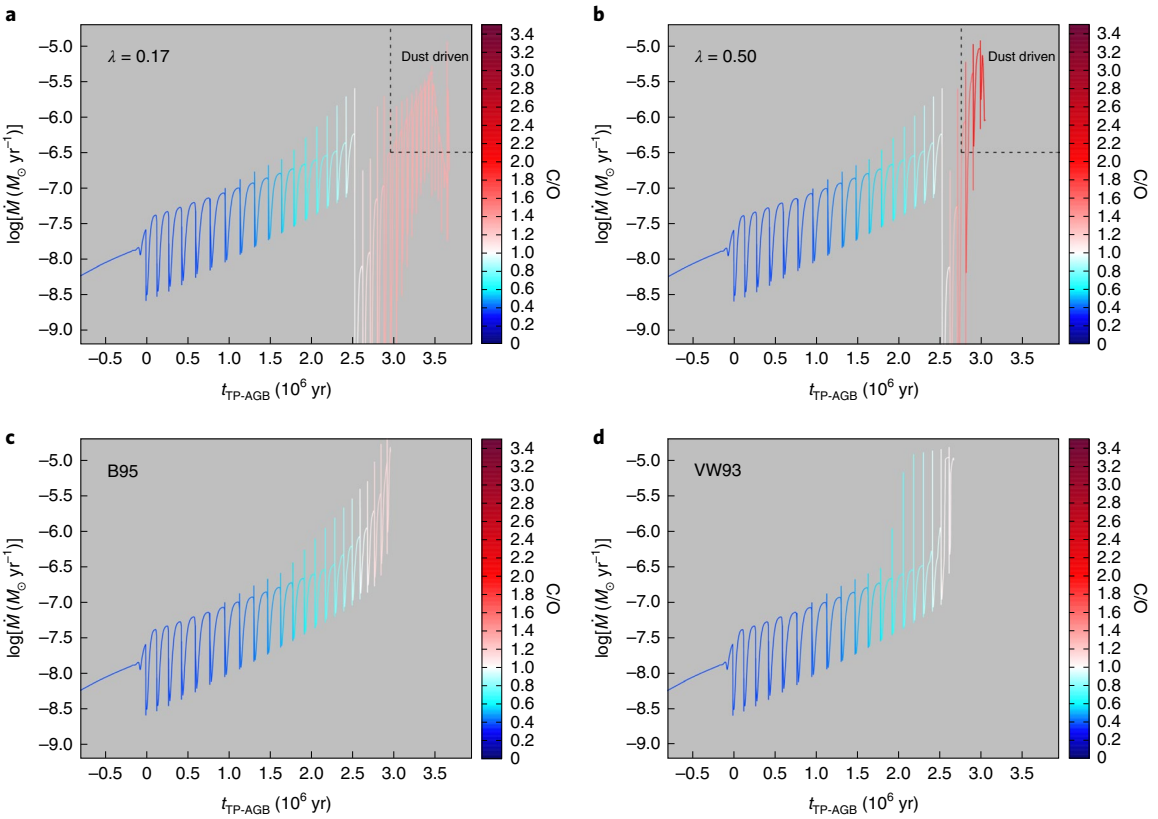

Fig. 2 | Evolution of the mass-loss rate during the whole TP-AGB evolution of a star with $M_i = 1.8\,M_\odot$ and solar metallicity. Time (t) is set to zero at the first TP. The tracks are colour-coded according to the current photospheric C/O ratio. Calculations differ in the treatment of mass loss and/or in the efficiency λ of the 3DU. **a**,**b**, Models in which mass loss during the carbon star phase does depend on the carbon excess (CDYN prescription; see Methods). The 3DU is less efficient in **a** compared with **b**. Inside the region delimited by the dotted lines, stellar winds are driven by carbonaceous dust grains. **c**,**d**, Results obtained with mass-loss formalisms that, unlike in **a** and **b**, do not contain an explicit dependence on the carbon abundance. See Methods for more details.

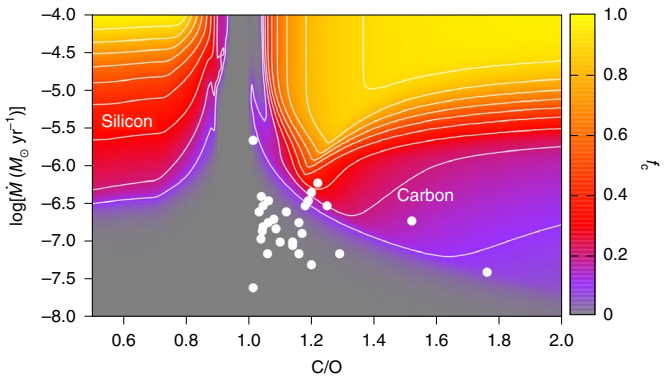

Fig. 3 | Map of the condensation factor, f_c, as a function of mass-loss rate and photospheric C/O. The assumed stellar parameters, $M = 1.5\ M_\odot$, $\log(L/L_\odot) = 3.85$, $T_{eff} = 2,950$ K, are extracted from the TP-AGB track (just before the 18th TP) of a model with $M_i = 1.8\,M_\odot$ and $Z = 0.014$. The quantity f_c refers to the fraction of silicon that condenses in silicates (olivine, pyroxene and quartz) for C/O < 1, while it corresponds to the condensed fraction of free carbon for C/O > 1. White dots show the location of a sample[29] of carbon-rich SRVs in the Milky Way with measured mass-loss rates and C/O. According to the map, most of these carbon stars should be dust free, in full agreement with their observed spectra[62].

region of the parameter space (M_i, λ), assuming solar initial metallicity. The results for the entire grid are shown in Extended Data Fig. 1a,b. We see that varying λ at a given M_i produces a large dispersion in the final WD mass and C/O. In particular, M_f of carbon stars anticorrelates with λ. At this point, the natural step is to pick up the (M_i, λ) combinations that best approximate the semi-empirical IFMR (Extended Data Fig. 1c,d).

The detected IFMR kink over the range $1.65 \lesssim M_i/M_\odot \lesssim 2.0$ is well recovered by assuming that these stars experience a shallow 3DU during the TP-AGB phase, typically with $0.1 \lesssim \lambda \lesssim 0.2$ (Extended Data Fig. 1c). Stars in the low-mass part ($1.65 \lesssim M_i/M_\odot < 1.8$) are those just massive enough to become carbon stars (Extended Data Fig. 1d). They are little enriched in carbon, with low final ratios ($1.1 \lesssim C/O \lesssim 1.2$) and low carbon excesses ($7.55 \lesssim C - O \lesssim 8.10$). In these models, carbonaceous dust grains are not expected to form in a sufficient amount to trigger a vigorous radiation-driven wind[21,32], while pulsation is likely to strip these stars of their small envelopes. The peak at $M_i \approx 1.8$–$1.9\,M_\odot$ corresponds to stars that reach a final C/O ≈ 1.3 when they overcome the minimum threshold, $(C - O)_{min} \approx 8.2$, late, close to the end of their evolution, and when the core has already grown appreciably in mass ($M_f \gtrsim 0.7\,M_\odot$).

Beyond the peak, at larger initial masses ($1.95 \lesssim M_i/M_\odot \lesssim 2.1$), the IFMR data are matched with TP-AGB models having a moderately higher efficiency, $0.2 \lesssim \lambda \lesssim 0.4$ (Extended Data Fig. 1c). Carbon enrichment is therefore somewhat larger and this leads to an earlier activation of the dust-driven wind. As a consequence, the WD masses are predicted to decrease until the IFMR regains a positive slope, as shown by the data for $M_i \geq 2.8\,M_\odot$ (Extended Data Fig. 1d). Models that reproduce this linear portion of the IFMR, with $2.6 \lesssim M_i/M_\odot \lesssim 3.5$, are characterized by a fairly higher efficiency of the 3DU, $0.5 \lesssim \lambda \lesssim 0.7$. They reach larger values of the final carbon

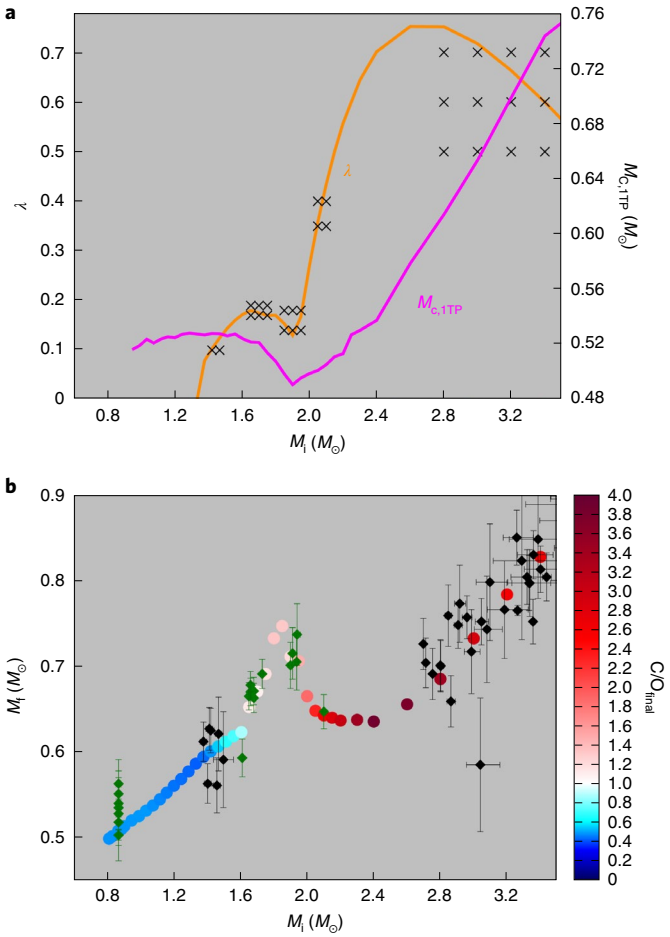

Fig. 4 | Calibration of the 3DU efficiency and the resulting theoretical IFMR. a, The values of the average λ (black crosses) that recover the semi-empirical IFMR data and a proposed best-fit curve for λ (orange line) as a function of the initial mass; the core mass at the first TP (magenta line). **b**, The theoretical IFMR obtained with the calibrated λ relation, colour-coded as a function of the final C/O (colour bar). The underlying semi-empirical IFMR (diamonds with errors bars) is the same as in Fig. 1, with the 7 newly discovered and 12 newly analysed WDs shown in green. Error bars cover a range of $\pm1\sigma$ (see Table 1).

excess ($8.7 \lesssim C-O \lesssim 9.2$) and carbon-to-oxygen ratio ($2 \lesssim C/O \lesssim 4$) so that dust grains are expected to condense plentifully in their extended atmospheres[21,22].

Using the ranges of λ just obtained, we may constrain the average efficiency of the 3DU as a function of M_i and derive the relation shown in Fig. 4a (orange curve). Adopting such a relation in our TP-AGB calculations, we get a theoretical IFMR that recovers quite well the semi-empirical data (Fig. 4b), in particular the peak around ~$1.8-1.9\,M_\odot$. We emphasize that the proposed calibration of the 3DU at solar metallicity is free from degeneracy with mass loss. In fact, in our TP-AGB models λ is the main free parameter, while the mass-loss rates for carbon stars do not contain any adjustable efficiency factor. Also, the effect of rotation should not play a substantial role in the IFMR over the M_i range of interest, unlike at higher masses ($M_i > 2.7\,M_\odot$)[33]. Finally, we stress that other models that adopt a much higher λ in TP-AGB stars with $M_i \lesssim 2\,M_\odot$, or mass-loss rates that do not depend on C−O, miss entirely the observed kink (Extended Data Fig. 2).

Looking at the calibrated 3DU relation (Fig. 4a), we see that λ is expected, on average, to increase with the stellar mass for $M_i \lesssim 3\,M_\odot$, a trend that is predicted by TP-AGB models in the literature[5]. Our analysis also indicates that this positive correlation is interrupted in two mass intervals.

In a narrow range around $M_i \approx 1.8-1.9\,M_\odot$, just where the peak of IFMR kink is placed, the data suggest the existence of a local slight minimum in λ. To interpret this result, we need to consider a few key aspects of stellar structure and evolution. The location of such a peak coincides with the initial mass limit, M_{HeF}, that divides the class of low-mass stars (characterized by electron degeneracy in the helium cores left at end of the hydrogen-burning phase and the subsequent helium flash at the tip of the RGB), from the class of intermediate-mass stars (with helium cores that obey the equation of state for the classical ideal gas). Stellar models show that such dichotomy in the equation of state leaves a fingerprint in the mass of the hydrogen-exhausted core, which reaches a minimum value at the stage of central helium ignition for $M_i = M_{HeF}$. This signature is retained also at later evolutionary stages, up to the onset of the TP-AGB phase. In fact, the core mass at the first TP, $M_{c,1TP}$, as a function of the initial mass (magenta curve), also exhibits a minimum at $M_i = M_{HeF}$ (refs. [5,34]).

From theory, we know that the core mass is a leading parameter of the TP-AGB evolution, and it is expected to affect the 3DU. In particular, lower values of M_c correspond to weaker TPs (measured by the post-flash luminosity peak)[35], hence shallow 3DU events. Consistent with this expectation, our calibration of the 3DU efficiency indicates that the minimum in λ occurs close to the minimum in $M_{c,1TP}$. At the same time, our evolutionary models predict that such a minimum characterizes the stellar progenitors of the observed IFMR kink. Putting these two findings together, we propose that the observed peak in WD mass was produced by Milky Way carbon stars with initial masses close to M_{HeF}, the transition limit between the classes of low- and intermediate-mass stars. These carbon stars experienced a modest carbon enrichment, an inefficient dust production, mild winds and a relatively long carbon-star phase.

The positive correlation between λ and M_i (Fig. 4a) breaks also at larger stellar masses, $M_i \gtrsim 3\,M_\odot$, where λ reaches a maximum and then starts to decrease. This latter trend is in line with some existing TP-AGB models[36,37] and earlier studies on the IFMR[8].

A few remarks about mass loss. Finally, we draw attention to a few aspects about the predicted mass-loss drop (Fig. 2). First, the amplitude of the drop also depends on the mass-loss rate attained during the phases with $C/O \lesssim 1$, immediately preceding the carbon star formation. If during these stages a dust-driven wind (involving silicate species, for instance) is not yet well developed, the size of the drop may be modest. The results shown here for $C/O < 1$ are based on a widely used, but likely simplistic, mass-loss formula[38]. While important progress has been recently made[39], new detailed stellar wind models for M- and S-type stars (including both SRV- and Mira-like pulsations) are highly desirable for future studies.

Second, it is worth specifying that in our evolutionary calculations we treat the mass-loss stages with $0.85 \lesssim C/O \lesssim 1$ in the same way as those with $C/O < 0.85$, since suitable wind models for S-type stars are still unavailable. Anyhow, a reasonable guess is that when C/O is quite close to unity while oxygen is still less abundant than carbon, a drop in mass loss may already occur due to the lack of ordinary silicates[24] (see also Fig. 3 for $C/O \lesssim 1$). This circumstance may explain the existence of S-type SRVs with mid-infrared blue colours, $K-[22] < 1$ (see cyan triangles in Supplementary Fig. 6 and related discussion; here [22] is the 22 μm band of the Wide-field Infrared Survey Explorer (WISE) space observatory).

Lastly and more importantly, the results presented here do not depend critically on the size of the mass-loss drop as long as the rates remain sufficiently low (below super-wind values). It makes little difference whether the rate is $10^{-10}\,M_\odot\,yr^{-1}$ or $10^{-7}\,M_\odot\,yr^{-1}$

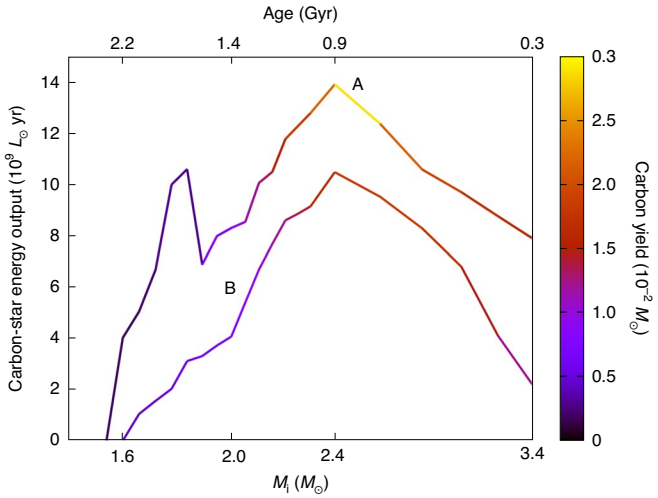

Fig. 5 | Integrated energy output emitted from the carbon-star phase. Predictions are derived by integrating the stellar luminosity along each track over the carbon-star lifetime. They are shown as a function of the initial stellar mass (bottom axis), and the corresponding age (top axis). Curve A refers to the present calibrated carbon star models (using the λ relation shown in Fig. 4a), and curve B shows the results obtained assuming a mass-loss recipe[38] insensitive to the surface chemical composition. The curves are colour-coded according to the yields of carbon newly synthesized during the TP-AGB phase.

given that, for typical interpulse periods of the order of 10^5 yr, the reduction of the envelope is small and the evolution proceeds temporarily almost at constant mass. What really matters is the onset of the dust-driven wind in carbon stars, which occurs when $C-O>(C-O)_{min}$ (depending on current values of luminosity (L), effective temperature (T_{eff}) and M). This is mainly controlled by the rapidity with which the atmosphere is enriched in carbon, therefore by the efficiency of the 3DU and the current envelope mass, which strengthens our λ calibration.

Summary and conclusions

A new thorough analysis of a few WDs in old open clusters with turn-off masses over the range from $1.6\,M_\odot \lesssim M_i \lesssim 2.1\,M_\odot$ has revealed that the IFMR exhibits a non-monotonic component, with a peak of $M_f \approx 0.70-0.75\,M_\odot$ at $M_i \approx 1.8-1.9\,M_\odot$. It happens just in proximity of the transition mass, at $M_i \approx M_{HeF}$, predicted by stellar structure models.

The proposed physical interpretation is that the IFMR kink marks the formation of solar-metallicity low-mass carbon stars. These latter experienced a shallow 3DU ($\lambda \approx 0.1-0.2$) during the TP-AGB phase, so that the amount of carbon dust available to trigger a radiation-driven wind was small and $\dot{M}$ remained mostly below a few $10^{-6}\,M_\odot\,yr^{-1}$. These circumstances led to a prolongation of the TP-AGB phase with the consequence that fairly massive WDs ($M_f > 0.65\,M_\odot$), larger than commonly expected, were left at the end of the evolution. The peak of the IFMR kink corresponds to the minimum in the 3DU efficiency ($\lambda \approx 0.1$), hence to the lowest carbon enrichment.

Considering the observed properties of carbon stars in the Milky Way, we suggest that the progenitors of the IFMR kink spent a fraction of their carbon star phase as SRVs, characterized by small-amplitude pulsations, low C/O, small mass-loss rates and low terminal velocities.

The observed nonlinearity of the IFMR at $M_i \approx 1.8-1.9\,M_\odot$ and its interpretation in terms of carbon star formation may have important consequences in the framework of galaxy evolution. In fact, the IFMR kink happens to occur just around a critical age, ~2 Gyr, which characterizes the oldest stellar populations hosted in galaxies at redshift larger than 3 and where carbon stars may appreciably contribute to the integrated galaxy light[40–42]. Figure 5 shows that the energy output from the carbon star phase at solar metallicity is higher than otherwise predicted by models that use mass-loss relations insensitive to the carbon abundance. In particular, the local peak in WD mass translates into a larger contribution from carbon stars, at ages around 1.5–2.0 Gyr, to the integrated light of galaxies similar to the Milky Way. Dedicated galaxy studies based on population synthesis models are needed to further investigate this aspect.

The impact on the chemical ejecta is also notable. Close to the WD mass peak, the amount of newly synthesized carbon expelled by stars with $1.6 \lesssim M_i/M_\odot \lesssim 1.9$ is quite low due to the little efficiency of the 3DU and the small envelope masses, while it increases by several factors for $M_i > 2\,M_\odot$. In conclusion, the progenitors that populate the IFMR kink are expected to be potentially important contributors to the galaxy emitted light and modest sources of carbon (in the form of gas and dust) at the same time.

Finally, we note that the IFMR kink has important consequences for the interpretation of the stellar progenitors of observed WDs in the mass range of $0.65 \lesssim M_f/M_\odot \lesssim 0.75$. Very common in the field and in binary systems, these WDs may have stellar progenitors with two, if not three, possible M_i.

Methods

White dwarf and cluster analyses. Gaia DR2[43,44] analysis of the NGC 752 and Ruprecht 147 clusters, with supplements from the deeper Canada–France–Hawaii Telescope (CFHT) photometry of Ruprecht 147[45], have been used to both identify WD candidates and their membership likelihood using proper motions and, for the brighter candidates, their parallaxes. Using two half nights of Keck I/Low Resolution Imaging Spectrometer (LRIS) analysis on 11 August and 8 September 2018, we observed ten WD candidates in Ruprecht 147 and one candidate in NGC 752. Eight of the ten observed Ruprecht 147 candidates were found to have hydrogen-rich atmospheres (WDs of type DA), one showed a helium-rich atmosphere (WD of type DB), and one is consistent with a background star. Observations of this DB's Hα region confirms that there is no hydrogen in its atmosphere. The one NGC 752 candidate is a DA. These WDs have been spectroscopically analysed using the standard DA[46] and updated DB[47,48] methods, and their spectroscopic-based T_{eff}, $\log g$ (where g is the surface gravity) and M_f are given in Table 1.

We then applied these spectroscopic parameters to the Montreal cooling models[49] to further test membership and single-star status using the luminosities, colours and cooling ages. Compared with the observed photometry, this tells us whether or not these WDs are consistent with being at the same distance, reddening and extinction as the cluster. In agreement with their proper motions and parallaxes, when available, the one NGC 752 DA and five of the Ruprecht 147 DAs and its one DB are consistent with single-star cluster membership. This DB is the first spectroscopically analysed DB with confirmed membership in a star cluster and it is has remarkable agreement in mass with the five Ruprecht 147 DAs at the same M_i. Even though we acknowledge that three-dimensional models should ideally be used in the spectroscopic analysis of DBs at these T_{eff} values[50], such three-dimensional corrections should be analysed in conjunction with updated van der Waals broadening[48]. However, it is reassuring that the DA and DB masses agree so well because we should expect that at these lower masses the DB IFMR is identical to that of DAs due to their consistent field mass distribution peaks[51].

Lastly, the three remaining observed Ruprecht 147 candidate DAs are at distances comparable to but not in agreement with the cluster. Their observed magnitudes are too faint rather than too bright relative to their spectroscopic-based luminosities, and hence they are also not potential binary cluster members. Moreover, all three have masses of ~0.60 $M_\odot$, inconsistent with the six confirmed members at ~0.67 $M_\odot$ and consistent with the most likely mass of WD field contaminants. Therefore, we consider them to be non-members.

In Supplementary Fig. 3, we photometrically analyse the cluster turnoffs using Gaia DR2-based cluster membership and Gaia photometry using our previously adopted cluster analysis techniques[15,52]. For consistent analysis with the presented evolutionary models of carbon star evolution, we derive M_i using both cluster ages and evolutionary timescales based on the PARSEC v1.2S + COLIBRI PR17 isochrones[53,54].

To expand on these spectroscopic techniques, we also take full advantage of the precise photometry, distances and extinctions available for both these WDs and their clusters. For the Ruprecht 147 and NGC 752 WDs, we adopt the Gaia

and CFHT photometry and our fit cluster parameters (Supplementary Fig. 3), and for the more distant NGC 6121 (metal-poor globular cluster M4), NGC 6819 and NGC 7789 WDs we adopt the Johnson BV photometry with our group's previously analysed cluster parameters[15]. When atmospheric composition is known, WD photometric-based parameters are precise with high-quality absolute magnitudes and colours, which are based on each WD's observed magnitudes corrected for cluster distance, extinction and reddening. However, photometry by itself is not able to determine atmospheric composition (unless ultraviolet filters are available), cluster membership or single-star status. In addition, our available colours of Johnson BV or Gaia's BP–RP provide only imprecise $T_{\rm eff}$ determinations at these high effective temperatures.

To overcome these challenges, here we have continued to use the strengths of spectroscopy to determine atmospheric composition, $T_{\rm eff}$, and spectroscopic mass, and the combination of these parameters with photometry to test membership and single-star status. However, these atmospheric compositions and spectroscopic $T_{\rm eff}$ are now then also combined with a WD's determined absolute magnitude to provide an independent measurement of WD radius, and hence mass, based on the Montreal cooling models.

This photometric mass is independent of the spectroscopic mass, even though its determination involves spectroscopic $T_{\rm eff}$, because the spectroscopic $T_{\rm eff}$ and spectroscopic $\log g$ errors are not correlated. In addition, while the conversion of $\log g$ to mass is $T_{\rm eff}$ dependent, it is weakly so at the moderate temperatures of these observed WDs. These photometric $M_{\rm f}$ determinations also show no signature of a systematic offset between each WD's spectroscopic $M_{\rm f}$. Therefore, our adopted $M_{\rm f}$ for each WD is a weighted combination of its photometric and spectroscopic mass (see Table 1 for each WD's absolute magnitude, photometric $M_{\rm f}$ and weighted-average $M_{\rm f}$). Furthermore, because these low-mass WDs at the tip of the cooling sequences in these old open clusters are expected to all have consistent mass, it is reassuring that this combination of photometric and spectroscopic information provides a remarkably consistent $M_{\rm f}$ for each cluster WD, more so than either the photometric or spectroscopic $M_{\rm f}$ results on their own. In constructing the weighted-average $M_{\rm f}$, the spectroscopic and photometric estimates, $M_{\rm f_S}$ and $M_{\rm f_P}$, are given a weight w that anticorrelates with the individual error, namely $w_{\rm S} = 1/\sigma_{\rm S}^2$ and $w_{\rm P} = 1/\sigma_{\rm P}^2$, respectively. The final error σ associated to each weighted-average $M_{\rm f}$ is obtained via the standard relation $\sigma = 1/\sqrt{\sigma_{\rm S}^{-2} + \sigma_{\rm P}^{-2}}$. As a consequence, the uncertainties of $M_{\rm f}$ are reduced. In particular, the scatter in $M_{\rm f}$ among the WDs belonging to NGC 7789, which populate the region close to the kink peak, shrinks considerably compared with previous work[15]. Lastly, Table 1 gives the cooling age and $M_{\rm i}$ resulting from this weighted-average $M_{\rm f}$.

These new semi-empirical IFMR data (see Table 1) have now been combined with WDs from our previous publication[15], which have also been more precisely analysed with the addition of their photometry. In addition, the WDs from M67[16,17] (with their $M_{\rm i}$ adjusted for consistency with our own PARSEC model fits of cluster age and evolutionary timescales) have been included. However, due to limitations with the available M67 WD photometry, only their spectroscopic WD parameters are used.

These low-mass WD data can be described with the fitting relations ($M_{\rm i}$ and $M_{\rm f}$ are in units of $M_{\odot}$):

$$M_{\rm f} = \begin{cases} 0.447 + 0.103\ M_{\rm i} & \text{if } 0.85 \lesssim M_{\rm i} \lesssim 1.51 \\ 0.001 + 0.399\ M_{\rm i} & \text{if } 1.51 < M_{\rm i} \lesssim 1.845 \\ 1.367 - 0.342\ M_{\rm i} & \text{if } 1.845 < M_{\rm i} \lesssim 2.21 \\ 0.210 + 0.181\ M_{\rm i} & \text{if } 2.21 < M_{\rm i} \lesssim 3.65 \end{cases}$$

See our previous publications[15,33] for the IFMR at masses of $M_{\rm i} > 3.65\,M_{\odot}$.

To establish the statistical significance of this kink, as illustrated in Fig. 1 and discussed here, we also rule out simpler IFMR fits of these low-mass IFMR data. We first test that the WD $M_{\rm f}$ errors are robust and are not underestimates. This is done by comparing the $M_{\rm f}$ errors to the intracluster $M_{\rm f}$ scatters, where at these lowest masses these WDs observed at the top of each cluster's cooling sequence can be assumed to have the same true $M_{\rm f}$ and $M_{\rm i}$. For NGC 6121, M67, Ruprecht 147 and NGC 7789, in each cluster 57% to 100% of the observed WD $M_{\rm f}$ are within their individual 1σ errors of their cluster weighted mean $M_{\rm f}$. For all clusters combined, 75% (18 out of 24) of the WDs are within 1σ of their cluster's $M_{\rm f}$ weighted mean. Normal error distributions are that ~68% of the data should be within 1σ of their distribution's mean. Therefore, the $M_{\rm f}$ errors are reliable and reproduce well the observed scatter.

Now that we have illustrated the robustness of the $M_{\rm f}$ errors, these errors act both as a weighting for the IFMR fits of these low-mass data and can illustrate how well various IFMR-fit shapes represent these data. A weighted linear fit of the low-mass data from $M_{\rm i}$ of 0.85 to $2.85\,M_{\odot}$ (purple line) creates a poor representation of the data where only 8 of the 26 (31%) low-mass WDs are within their 1σ errors of this linear fit, where again we should expect ~68% to be for a representative fit. This fit also only gives a reduced chi-squared of 2.57, representative of under-fitting the data.

The next level of complexity for fitting these data is a weighted linear fit from 0.85 to $2.15\,M_{\odot}$ (magenta line), or comparably from 0.85 to $2.00\,M_{\odot}$ (excluding NGC 752-WD01; blue line). However, like with our adoption of a kinked fit, both of these cases must still then be followed by a temporarily decreasing IFMR to match back with the Hyades WDs at $M_{\rm i}$ of $2.7\,M_{\odot}$ and to not overproduce $0.7\,M_{\odot}$ WDs in the field. This latter point is illustrated in the Supplementary Section 'The WD mass distribution' and Supplementary Figs. 1 and 2. With both fits, 19 of the 26 (73%) and 19 out of 25 (76%) low-mass WDs are now within their 1σ errors of these fits, but they are still unlikely representations of the data because these fits overestimate the mass of nearly every M67, NGC 6819 and NGC 752 WD while they underestimate the mass of nearly every Ruprecht 147 and NGC 7789 WD. Such clumpy (non-random) residuals are extremely unlikely for a fit that well represents the data. For reference, the reduced chi-squared values of these two fits are 1.88 and 1.09, respectively, the latter of which does not rule out its goodness of fit, but again the clumpy residuals argue against this being representative of the data.

Finally, the low-mass IFMR ($M_{\rm i} < 2.21\,M_{\odot}$) is described with the three-piece kink fit given above (black line), which connects to the intermediate-mass $2.21 < M_{\rm i} \lesssim 3.65$ and higher-mass IFMR discussed in greater detail in our previous work[15,33]. In addition, where the data remain limited between $M_{\rm i}$ of $2.0\,M_{\odot}$ and $2.7\,M_{\odot}$, the fit is partially guided by the model in Fig. 4b. This three-piece kink is the simplest fit that can both match the current IFMR data and produce appropriately random residuals (20 of the 26 data WDs (77%) being within 1σ of the fit and with a reassuring reduced chi-squared of 1.02). At the same time, the kink IFMR fit proves to be consistent with the field WD mass distribution in the Milky Way (Supplementary Fig. 2e). Clearly, further IFMR data for $2.0 \lesssim M/M_{\odot} \lesssim 2.7$ will be valuable, but the existence of an IFMR kink is becoming established.

Stellar evolution models. We computed a set of TP-AGB models with the COLIBRI code[34], for 42 selected values of the initial mass in the range $0.8 \lesssim M_{\rm i}/M_{\odot} \lesssim 3.4$, assuming a solar-like initial metallicity[55], $Z = 0.014$. We recall that, according to standard terminology, Z denotes the total abundance (in mass fraction) of all elements heavier than helium. The initial conditions at the first TP are taken from a grid of PARSEC tracks[53]. A key aspect of the TP-AGB models is the integration of the ÆSOPUS code[23] inside COLIBRI. This allows to calculate on-the-fly both the equation of state for about 800 atomic and molecular species and the Rosseland mean gas opacities (for temperatures $2{,}500\,{\rm K} \lesssim T \lesssim 15{,}000\,{\rm K}$). In this way, the effects of abundance changes, due to mixing events, on the atmospheric structure can be treated in detail.

On the red giant branch, mass loss is computed using the Reimers law[56], with an efficiency parameter $\eta_{\rm R} = 0.2$. Later, the AGB mass loss by stellar winds is described as a two-stage process[57]. During the early phases, for luminosities below the tip of the red giant branch ($\log(L/L_{\odot}) \approx 3.4 - 3.5$), we assume that mass loss is driven by Alfvén waves in cool and extended chromospheres[58]. Later, as long-period variability develops and the star becomes luminous and cool enough, powerful winds are accelerated by radiation pressure on dust grains that condense in the outer layers of the pulsating atmospheres. In the dust-driven regime, the mass-loss rate is computed with different prescriptions according to the surface C/O ratio, namely: a widely used relation[38] (with an efficiency parameter $\eta_{\rm B} = 0.01$; B95 in the text) based on dynamical calculations of the atmospheres of Mira-like stars for the O-rich stages when C/O < 1, and a routine based on state-of-the-art dynamical atmosphere models[21,22] for carbon stars when C/O > 1 (also referred to as CDYN in the text). These models, in particular, predict that dust-driven winds in carbon stars are activated only when (1) the amount of free carbon, C − O, exceeds a threshold $({\rm C-O})_{\rm min}$, and (2) favourable conditions exist in the extended atmospheres for condensation of dust grains. Inside the grid of wind models for carbon stars adopted here, the threshold in carbon excess is predicted to vary within a range, $8.2 \lesssim ({\rm C-O})_{\rm min} \lesssim 9.1$, the exact value depending on other stellar parameters, namely mass, luminosity and effective temperature. At solar-like metallicity, $Z = 0.014$, assuming that oxygen is not altered by the 3DU, such a range in $({\rm C-O})_{\rm min}$ translates into a range of the minimum C/O required for radiation-driven winds, $1.3 \lesssim ({\rm C/O})_{\rm min} \lesssim 2.7$.

As long as suitable conditions for the activation of the dust-driven wind are not fulfilled, typically during the early stages of carbon stars (characterized by low C − O, low L/M ratios and relatively high $T_{\rm eff}$) the CDYN prescription cannot be applied. In these cases, we reasonably assume that stellar winds are sustained by pulsations alone[32]. Pulsation-driven mass loss is described by fitting a set of dynamical models for dust-free atmospheres[59], and expressing the mass-loss rate ($M_{\odot}\,{\rm yr}^{-1}$) with the form[60] $\dot{M} = \exp(a\ M^b R^c)$, where M and R denote the star's mass and radius in solar units ($a = -789$, $b = 0.558$ and $c = -0.676$). The resulting rates are typically low, from $\sim 10^{-9}$–$10^{-7}\,M_{\odot}\,{\rm yr}^{-1}$, but values of $\sim 10^{-6}\,M_{\odot}\,{\rm yr}^{-1}$ can be reached for suitable combinations of stellar mass, luminosity and effective temperature.

The set of mass-loss prescriptions described above constitutes our standard choice for the models presented in this work. For the purpose of discussion, we also apply to carbon stars additional options that do not depend on the photospheric C/O, namely: the B95 formula or the semi-empirical formalism[61] (VW93 in the text) that relates the mass-loss rate to the fundamental-mode period of pulsating AGB stars.

The 3DU is described with a parametric approach[34] that determines the onset and the quenching of the mixing events, and their efficiency λ. A 3DU episode takes place when a temperature criterion is met, that is, provided the temperature at the base of the convective envelope exceeds a minimum value, $T_{\rm b}^{\rm dred}$, at the stage of the post-flash luminosity maximum. We adopt[34] $\log T_{\rm b}^{\rm dred} = 6.4$.

To perform a systematic exploration of the effect of the 3DU efficiency on the IFMR, similarly to the approach introduced in an earlier study[8], we ran a large grid of TP-AGB models varying λ from 0.05 to 0.7 in steps of 0.05 or 0.1, for all values of M_i under consideration. To avoid additional free parameters in the description of the 3DU, we make the simple assumption that the efficiency λ is constant during the TP-AGB phase as long as the temperature criterion with T_b^{dred} is fulfilled. Therefore, the values of λ should be considered as a measure of the average efficiency of the 3DU experienced by a star of given initial mass.

The results are shown in Extended Data Fig. 1. We see that a sizeable scatter is produced, as a consequence of the changes in both core mass and surface chemical composition. The case $\lambda = 0.05$ does not form any carbon star at any M_i. As to the models with final C/O > 1 we see that, on average, increasing λ results in less-massive WDs at a given M_i. The reason is twofold. On one side, a more efficient 3DU reduces the net core-mass growth (by an amount $\lambda \times \Delta M_c$ at each mixing event). On the other side, it enriches the atmosphere with more carbon, which favours the onset of the dust-driven wind with consequent earlier termination of the TP-AGB phase. The present model grid is used to calibrate λ as a function of M_i, as discussed in the main text.

Data availability

The data that support the plots within this paper and other findings of this study are available from the corresponding author upon reasonable request. Montreal WD cooling models are publicly available from http://www.astro.umontreal.ca/~bergeron/CoolingModels. The pulsation periods are computed with fitting relations based on publicly available models that can be found at http://starkey.astro.unipd.it/pulsation_models.html.

Code availability

The stellar evolution codes PARSEC and COLIBRI are not publicly available. The mass-loss routine for carbon stars can be found at https://www.astro.uu.se/coolstars/TOOLS/MLR-routines/C/. The code to compute the dust-grain growth in the outflows of AGB stars can be retrieved from http://www.ita.uni-heidelberg.de/~gail/agbdust/agbdust.html. The code used here to calculate photometry-based WD parameters is available from https://github.com/SihaoCheng/WD_models.

Received: 13 March 2019; Accepted: 20 May 2020;
Published online: 6 July 2020

References

1. Cescutti, G., Matteucci, F., McWilliam, A. & Chiappini, C. The evolution of carbon and oxygen in the bulge and disk of the Milky Way. *Astron. Astrophys.* **505**, 605–612 (2009).
2. Gustafsson, B., Karlsson, T., Olsson, E., Edvardsson, B. & Ryde, N. The origin of carbon, investigated by spectral analysis of solar-type stars in the Galactic Disk. *Astron. Astrophys.* **342**, 426–439 (1999).
3. Mattsson, L. The origin of carbon: low-mass stars and an evolving, initially top-heavy IMF? *Astron. Astrophys.* **515**, A68 (2010).
4. Bensby, T. & Feltzing, S. The origin and chemical evolution of carbon in the galactic thin and thick discs. *Mon. Not. R. Astron. Soc.* **367**, 1181–1193 (2006).
5. Karakas, A. I. & Lattanzio, J. C. The Dawes Review 2: nucleosynthesis and stellar yields of low- and intermediate-mass single stars. *Publ. Astron. Soc. Aus.* **31**, e030 (2014).
6. Herwig, F. Evolution of asymptotic giant branch stars. *Annu. Rev. Astron. Astrophys.* **43**, 435–479 (2005).
7. Salaris, M., Serenelli, A., Weiss, A. & Miller Bertolami, M. Semi-empirical white dwarf initial–final mass relationships: a thorough analysis of systematic uncertainties due to stellar evolution models. *Astrophys. J.* **692**, 1013–1032 (2009).
8. Kalirai, J. S., Marigo, P. & Tremblay, P.-E. The core mass growth and stellar lifetime of thermally pulsing asymptotic giant branch stars. *Astrophys. J.* **782**, 17 (2014).
9. Bird, J. C. & Pinsonneault, M. H. A bound on the light emitted during the thermally pulsing asymptotic giant branch phase. *Astrophys. J.* **733**, 81 (2011).
10. Marigo, P. & Girardi, L. Coupling emitted light and chemical yields from stars: a basic constraint to population synthesis models of galaxies. *Astron. Astrophys.* **377**, 132–147 (2001).
11. Weidemann, V. Revision of the initial-to-final mass relation. *Astron. Astrophys.* **363**, 647–656 (2000).
12. Kalirai, J. S. et al. The initial–final mass relation: direct constraints at the low-mass end. *Astrophys. J.* **676**, 594–609 (2008).
13. Cummings, J. D., Kalirai, J. S., Tremblay, P.-E. & Ramirez-Ruiz, E. Two massive white dwarfs from NGC 2323 and the initial–final mass relation for progenitors of 4 to 6.5 $M_\odot$. *Astrophys. J.* **818**, 84 (2016).
14. Kalirai, J. S. et al. The masses of population II white dwarfs. *Astrophys. J.* **705**, 408–425 (2009).
15. Cummings, J. D., Kalirai, J. S., Tremblay, P.-E., Ramirez-Ruiz, E. & Choi, J. The white dwarf initial–final mass relation for progenitor stars from 0.85 to 7.5 $M_\odot$. *Astrophys. J.* **866**, 21 (2018).
16. Williams, K. A. et al. Ensemble properties of the white dwarf population of the old, solar metallicity open star cluster Messier 67. *Astrophys. J.* **867**, 62 (2018).
17. Canton, P. *The Initial–Final Mass Relation Revisited: A Monte Carlo Approach with the Addition of the M67 White Dwarf Population*. PhD thesis, Univ. Oklahoma (2018).
18. Tremblay, P.-E. et al. The field white dwarf mass distribution. *Mon. Not. R. Astron. Soc.* **461**, 2100–2114 (2016).
19. El-Badry, K., Rix, H.-W. & Weisz, D. R. An empirical measurement of the initial–final mass relation with Gaia white dwarfs. *Astrophys. J. Lett.* **860**, L17 (2018).
20. Bladh, S., Eriksson, K., Marigo, P., Liljegren, S. & Aringer, B. Carbon star wind models at solar and sub-solar metallicities: a comparative study. I. Mass loss and the properties of dust-driven winds. *Astron. Astrophys.* **623**, A119 (2019).
21. Eriksson, K., Nowotny, W., Höfner, S., Aringer, B. & Wachter, A. Synthetic photometry for carbon-rich giants. IV. An extensive grid of dynamic atmosphere and wind models. *Astron. Astrophys.* **566**, A95 (2014).
22. Mattsson, L., Wahlin, R. & Höfner, S. Dust driven mass loss from carbon stars as a function of stellar parameters. I. A grid of solar-metallicity wind models. *Astron. Astrophys.* **509**, A14 (2010).
23. Marigo, P. & Aringer, B. Low-temperature gas opacity. ÆSOPUS: a versatile and quick computational tool. *Astron. Astrophys.* **508**, 1539–1569 (2009).
24. Ferrarotti, A. S. & Gail, H. P. Mineral formation in stellar winds. III. Dust formation in S stars. *Astron. Astrophys.* **382**, 256–281 (2002).
25. Ferrarotti, A. S. & Gail, H.-P. Composition and quantities of dust produced by AGB-stars and returned to the interstellar medium. *Astron. Astrophys.* **447**, 553–576 (2006).
26. Dell'Agli, F. et al. Asymptotic giant branch and super-asymptotic giant branch stars: modelling dust production at solar metallicity. *Mon. Not. R. Astron. Soc.* **467**, 4431–4440 (2017).
27. Nanni, A., Bressan, A., Marigo, P. & Girardi, L. Evolution of thermally pulsing asymptotic giant branch stars—II. Dust production at varying metallicity. *Mon. Not. R. Astron. Soc.* **434**, 2390–2417 (2013).
28. Höfner, S. & Olofsson, H. Mass loss of stars on the asymptotic giant branch. Mechanisms, models and measurements. *Astron. Astrophys. Rev.* **26**, 1 (2018).
29. Schöier, F. L. & Olofsson, H. Models of circumstellar molecular radio line emission. Mass loss rates for a sample of bright carbon stars. *Astron. Astrophys.* **368**, 969–993 (2001).
30. McDonald, I., De Beck, E., Zijlstra, A. A. & Lagadec, E. Pulsation-triggered dust production by asymptotic giant branch stars. *Mon. Not. R. Astron. Soc.* **481**, 4984–4999 (2018).
31. McDonald, I. & Trabucchi, M. The onset of the AGB wind tied to a transition between sequences in the period-luminosity diagram. *Mon. Not. R. Astron. Soc.* **484**, 4678–4682 (2019).
32. Winters, J. M., Le Bertre, T., Jeong, K. S., Helling, C. & Sedlmayr, E. A systematic investigation of the mass loss mechanism in dust forming long-period variable stars. *Astron. Astrophys.* **361**, 641–659 (2000).
33. Cummings, J. D. et al. A novel approach to constrain rotational mixing and convective-core overshoot in stars using the initial–final mass relation. *Astrophys. J.* **871**, L18 (2019).
34. Marigo, P., Bressan, A., Nanni, A., Girardi, L. & Pumo, M. L. Evolution of thermally pulsing asymptotic giant branch stars—I. The COLIBRI code. *Mon. Not. R. Astron. Soc.* **434**, 488–526 (2013).
35. Wagenhuber, J. & Groenewegen, M. A. T. New input data for synthetic AGB evolution. *Astron. Astrophys.* **340**, 183–195 (1998).
36. Ventura, P., Karakas, A., Dell'Agli, F., García-Hernández, D. A. & Guzman-Ramirez, L. Gas and dust from solar metallicity AGB stars. *Mon. Not. R. Astron. Soc.* **475**, 2282–2305 (2018).
37. Cristallo, S., Straniero, O., Piersanti, L. & Gobrecht, D. Evolution, nucleosynthesis, and yields of AGB stars at different metallicities. III. Intermediate-mass models, revised low-mass models, and the ph-FRUITY interface. *Astrophys. J. Suppl.* **219**, 40 (2015).
38. Bloecker, T. Stellar evolution of low and intermediate-mass stars. I. Mass loss on the AGB and its consequences for stellar evolution. *Astron. Astrophys.* **297**, 727–738 (1995).
39. Bladh, S., Liljegren, S., Höfner, S., Aringer, B. & Marigo, P. An extensive grid of DARWIN models for M-type AGB stars. I. Mass-loss rates and other properties of dust-driven winds. *Astron. Astrophys.* **626**, A100 (2019).
40. Girardi, L., Marigo, P., Bressan, A. & Rosenfield, P. The insidious boosting of thermally pulsing asymptotic giant branch stars in intermediate-age magellanic cloud clusters. *Astrophys. J.* **777**, 142 (2013).
41. Maraston, C. et al. Evidence for TP-AGB stars in high-redshift galaxies, and their effect on deriving stellar population parameters. *Astrophys. J.* **652**, 85–96 (2006).

42. Bruzual, A. & Charlot, G. Spectral evolution of stellar populations using isochrone synthesis. *Astrophys. J.* **405**, 538–553 (1993).
43. Gaia Collaboration et al. The Gaia mission. *Astron. Astrophys.* **595**, A1 (2016).
44. Gaia Collaboration et al. Gaia Data Release 2. Summary of the contents and survey properties. *Astron. Astrophys.* **616**, A1 (2018).
45. Curtis, J. L., Wolfgang, A., Wright, J. T., Brewer, J. M. & Johnson, J. A. Ruprecht 147: the oldest nearby open cluster as a new benchmark for stellar astrophysics. *Astron. J.* **145**, 134 (2013).
46. Tremblay, P.-E., Bergeron, P. & Gianninas, A. An improved spectroscopic analysis of DA white dwarfs from the Sloan Digital Sky Survey Data Release 4. *Astrophys. J.* **730**, 128 (2011).
47. Bergeron, P. et al. A comprehensive spectroscopic analysis of DB white dwarfs. *Astrophys. J.* **737**, 28 (2011).
48. Genest-Beaulieu, C. & Bergeron, P. A comprehensive spectroscopic and photometric analysis of DA and DB white dwarfs from SDSS and Gaia. *Astrophys. J.* **871**, 169 (2019).
49. Fontaine, G., Brassard, P. & Bergeron, P. The potential of white dwarf cosmochronology. *Publ. Astron. Soc. Pac.* **113**, 409–435 (2001).
50. Cukanovaite, E., Tremblay, P.-E., Freytag, B., Ludwig, H.-G. & Bergeron, P. Pure-helium 3D model atmospheres of white dwarfs. *Mon. Not. R. Astron. Soc.* **481**, 1522–1537 (2018).
51. Tremblay, P. E., Cukanovaite, E., Gentile Fusillo, N. P., Cunningham, T. & Hollands, M. A. Fundamental parameter accuracy of DA and DB white dwarfs in Gaia data release 2. *Mon. Not. R. Astron. Soc.* **482**, 5222–5232 (2019).
52. Cummings, J. D. & Kalirai, J. S. Improved main-sequence turnoff ages of young open clusters: multicolor UBV techniques and the challenges of rotation. *Astron. J.* **156**, 165 (2018).
53. Bressan, A. et al. PARSEC: stellar tracks and isochrones with the PAdova and TRieste stellar evolution code. *Mon. Not. R. Astron. Soc.* **427**, 127–145 (2012).
54. Marigo, P. et al. A new generation of PARSEC-COLIBRI stellar isochrones including the TP-AGB phase. *Astrophys. J.* **835**, 77 (2017).
55. Asplund, M., Grevesse, N., Sauval, A. J. & Scott, P. The chemical composition of the Sun. *Annu. Rev. Astron. Astrophys.* **47**, 481–522 (2009).
56. Reimers, D. Circumstellar absorption lines and mass loss from red giants. *Mem. Soc. R. Sci. Liege* **8**, 369–382 (1975).
57. Pastorelli, G. et al. Constraining the thermally pulsing asymptotic giant branch phase with resolved stellar populations in the small magellanic cloud. *Mon. Not. R. Astron. Soc.* **485**, 5666–5692 (2019).
58. Cranmer, S. R. & Saar, S. H. Testing a predictive theoretical model for the mass loss rates of cool stars. *Astrophys. J.* **741**, 54 (2011).
59. Bowen, G. H. Dynamical modeling of long-period variable star atmospheres. *Astrophys. J.* **329**, 299–317 (1988).
60. Bedijn, P. J. Pulsation, mass loss, and evolution of upper asymptotic giant branch stars. *Astron. Astrophys.* **205**, 105–124 (1988).
61. Vassiliadis, E. & Wood, P. R. Evolution of low- and intermediate-mass stars to the end of the asymptotic giant branch with mass loss. *Astrophys. J.* **413**, 641–657 (1993).
62. Lambert, D. L., Gustafsson, B., Eriksson, K. & Hinkle, K. H. The chemical composition of carbon stars. I—Carbon, nitrogen, and oxygen in 30 cool carbon stars in the galactic disk. *Astrophys. J. Suppl.* **62**, 373–425 (1986).

Acknowledgements

P.M., S.B., Y.C., L.G., G.P., M.T. and B.A. acknowledge the support from the ERC Consolidator Grant funding scheme (project STARKEY, grant agreement number 615604). P.-E.T. has received ERC funding under the European Union's Horizon 2020 research and innovation programme (grant agreement number 677706 – WD3D).

Author contributions

P.M. designed and performed the theoretical research, ran the TP-AGB models and the population synthesis simulations, and provided the interpretation of the new IFMR data in terms of stellar evolution. J.D.C. performed the Keck observations, processed the data, analysed the cluster parameters, spectroscopically analysed the DA WDs and determined memberships. J.L.C. identified the likely WD candidates for observations and assisted with the cluster-parameter analysis. J.K. coordinated the observational and theoretical work and provided expertise. P.-E.T. provided the DA WD atmospheric models and fitting program and his expertise. E.R.-R. assisted with Keck observations. P.B. provided the DB WD atmospheric models and fit the DB parameters. S.B. provided expertise and help in implementing the mass-loss grid of dynamical atmospheres for carbon stars in the COLIBRI code. Y.C., A.B., L.G., G.P. and M.T. contributed to the development of the stellar models and the discussion of the results. S.C. contributed his WD photometric analysis expertise and his publicly available Python 3 module was used for the photometric-based derivation of WD parameters. B.A. provided expertise and the molecular opacity data to model the atmospheres of carbon stars. P.D.T. implemented the WD models in the populations synthesis simulations.

Competing interests

The authors declare no competing interests.

Additional information

Extended data is available for this paper at https://doi.org/10.1038/s41550-020-1132-1.

Supplementary information is available for this paper at https://doi.org/10.1038/s41550-020-1132-1.

Correspondence and requests for materials should be addressed to P.M.

Peer review information *Nature Astronomy* thanks Krzysztof Gesicki, Iain McDonald and the other, anonymous, reviewer(s) for their contribution to the peer review of this work.

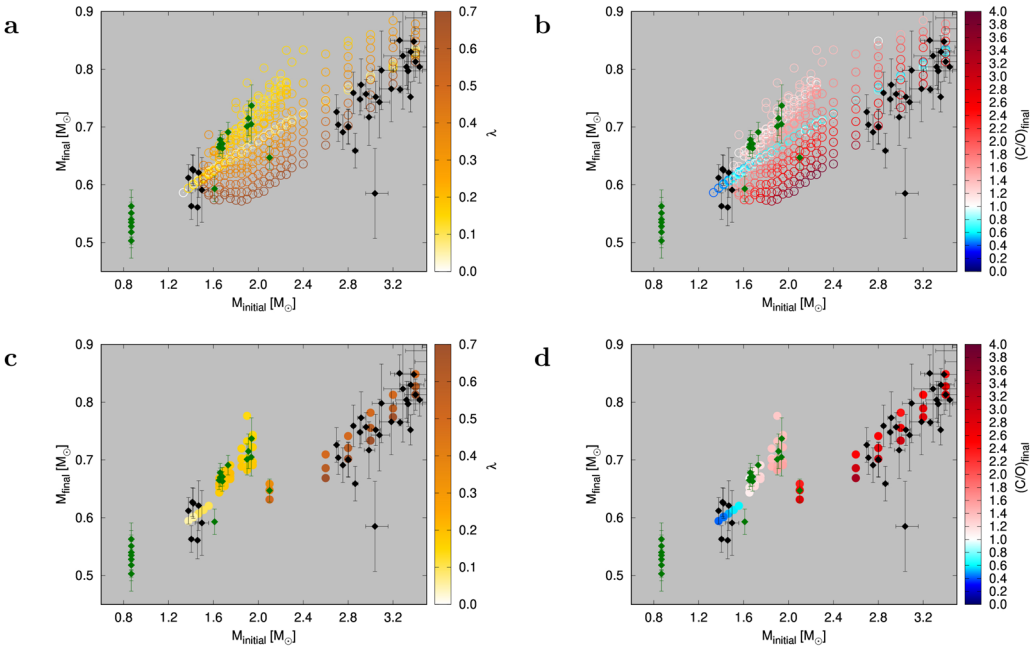

Extended Data Fig. 1 | Comparison between the semi-empirical IFMR and model results. The semi-empirical data are shown with diamonds and error bars covering the range of $\pm 1\,\sigma$. Newly discovered and newly analysed WD data (see Table 1) are shown in green. **a**-**b**, Predictions for the whole (M_i, λ) grid of models. **c**-**d**, Selected models that are found to match the semi-empirical IFMR. The theoretical IFMR is colour-coded according to the values of the efficiency of the 3DU (**a**-**c**) and the photospheric C/O at the end of the TP-AGB phase (**b**-**d**).

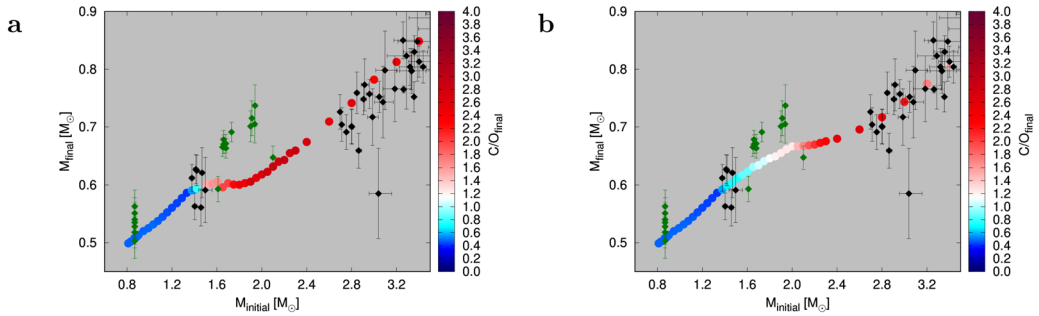

Extended Data Fig. 2 | Examples of theoretical IFMRs that fail to account for the kink in the semi-empirical IFMR. a, Too high efficiency of the 3DU in low-mass stars: $\lambda = 0.5$ is assumed for all models that experience the 3DU. **b**, Mass loss insensitive to the photospheric chemical composition: the B95 mass-loss formula is applied to all models, irrespective of the photospheric C/O. The semi-empirical IFMR is the same as in Fig. 1, with error bars covering the range of $\pm 1\,\sigma$.